Nanotechnology, Science and Applications

Dovepress
Taylor & Francis Group

Open Access Full Text Article

ORIGINAL RESEARCH

Revisiting Physicochemical and Biological Properties of Zn^{2+} - Enriched Hydroxyapatite

Łukasz Pajchel[1], Monika Budnicka[1], Milena Wawryniuk[2], Roman Grygoruk[3], Ewa Bednarczyk[3], Joanna Kolmas[1]

[1]Department of Pharmaceutical Chemistry and Biomaterials, Faculty of Pharmacy, Medical University of Warsaw, Warsaw, Poland; [2]Department of Toxicology and Bromatology, Faculty of Pharmacy, Medical University of Warsaw, Warsaw, Poland; [3]Department of Construction Engineering and Biomedical Engineering, Faculty of Mechanical and Industrial Engineering, Warsaw University of Technology, Warsaw, Poland

Correspondence: Joanna Kolmas, Department of Pharmaceutical Chemistry and Biomaterials, Faculty of Pharmacy, Medical University of Warsaw, Banacha 1 str, Warsaw, 02-097, Poland, Email joanna.kolmas@wum.edu.pl

Purpose: This nanotechnology-oriented study provides insights into the nanoscale structural and compositional modulation of hydroxyapatite. This study investigated the effect of zinc ions (Zn^{2+}) content (0–1.8 mol%) in nanocrystalline hydroxyapatite on its physicochemical and biological properties, focusing on biomedical applications.

Materials and Methods: A series of zinc-enriched nanocrystalline hydroxyapatites was synthesized via aqueous precipitation. Their ultrastructure and crystallinity were characterized by transmission electron microscopy (TEM) and powder X-ray diffraction (PXRD), including unit cell analysis. Chemical composition—specifically OH^-, HPO_4^{2-}, and CO_3^{2-} groups—was examined using Fourier transform infrared spectroscopy (FT-IR), Raman spectroscopy, and solid-state nuclear magnetic resonance (ssNMR). Zn^{2+} content and release over seven weeks were quantified via flame atomic absorption spectrometry (F-AAS). Cytotoxicity was evaluated using MTT and NRU assays.

Results: Increasing Zn^{2+} concentration led to reduced crystal size and crystallinity. Zinc ions were incorporated both into the crystalline core and the hydrated surface layer of hydroxyapatite. At concentrations ≥1.0 mol%, an amorphous zinc phosphate phase appeared. Higher Zn^{2+} levels also correlated with decreased hydroxyl groups and carbonate impurities, accompanied by increased water content and acidic phosphate groups. Zinc ion release remained minimal across all samples, independent of the initial zinc concentration. Cytotoxicity assays revealed that samples containing 0–0.6 mol% Zn^{2+} were non-toxic, while those with 1.0 mol% and 1.8 mol% Zn^{2+} exhibited cytotoxic effects.

Conclusion: Zn-doped hydroxyapatite containing up to 0.6 mol% Zn^{2+} exhibits enhanced structural stability and cytocompatibility, establishing 0.6 mol% as the optimal threshold for biomedical applications.

Keywords: zinc, nanocrystalline calcium phosphates, physicochemical analysis, ion release, chemical structure

Introduction

Hydroxyapatite (HA) has attracted the interest of researchers for many years, not only geologists and geochemists but also biologists, biomaterials engineers, orthopedic surgeons, and dentists.[1–3] HA with chemical composition ($Ca_{10}(PO_4)_6(OH)_2$) is both a naturally occurring mineral in igneous rocks and chemically similar to the mineral phase of bone, dentin, and enamel.[3,4] Synthetic HA is a valuable bone substitute material. It supports osseointegration when applied as a coating on polymeric and metallic implants, ensures biocompatibility and bioactivity in composite materials, and serves as an innovative carrier for active substances in bone tissue engineering.[5–8]

A critical feature of HA in biomedical applications is its ability to undergo ionic substitutions.[8,9] Calcium, phosphate, and hydroxyl ions in the crystalline structure of HA can be partially replaced by ions of similar size, shape, and charge. Biological apatite, which constitutes mineralized tissues, is essentially a multi-substituted HA.[10,11] Divalent cations such as magnesium, manganese, and zinc, as well as monovalent cations like sodium and potassium, often replace calcium. Similarly, phosphate ions can be substituted with silicate or carbonate ions, while hydroxyl groups may be replaced by chloride, fluoride, or carbonate ions. Ionic substitutions can lead to various structural effects. When ions of different valencies are involved, charge

Received: 7 June 2025
Accepted: 24 October 2025
Published: 12 November 2025

compensation is required, whereas differences in ionic radius or shape may influence unit cell dimensions and crystal size. Incorporating foreign ions into the HA structure allows for modifications in its physicochemical (eg, solubility, thermal stability, adsorption capacity) and mechanical properties.[12,13] However, the most intriguing aspect in the context of bone biomaterials is the alteration of biological properties. For example, the incorporation of silicate or magnesium ions enhances bone tissue formation around implants, while silver or copper ions impart antibacterial properties.[14–17] Additionally, strontium ions promote osteoblast proliferation while simultaneously inhibiting osteoclast activity.[18] It is also well established that nanocrystalline apatites consist of a crystalline core surrounded by a hydrated surface layer. This surface layer, which readily accommodates labile ions, plays a key role in biological interactions and osseointegration.[11]

In this study, we focused on re-examining zinc-substituted HA. Zinc is an essential trace element crucial for bone tissue development and homeostasis.[19,20] It is not only a component of bone tissue but also plays a role in collagen matrix synthesis, mineralization, and bone turnover. Studies have shown that zinc stimulates the transcription factor Runx2, thereby promoting osteoblast differentiation. Conversely, zinc inhibits osteoclastogenesis and reduces bone resorption by inducing osteoclast apoptosis. Moreover, zinc modulates the RANKL/RANK/OPG signaling pathway, thereby facilitating bone remodelling.[21]

Numerous studies have investigated zinc-substituted HA.[22–31] However, several key aspects remain unclear. One of the unresolved issues is the effect of varying zinc content on the crystallinity of HA and the formation of amorphous phases. Additionally, conflicting data exist regarding the substitution limit of zinc ions and the precise mechanisms of their incorporation into the HA structure. Furthermore, only a limited number of studies have addressed the release kinetics of zinc ions from HA materials.[25,28] It should also be noted that zinc substitution may introduce certain limitations, such as reduced thermal stability and potential cytotoxicity at higher concentrations.[30,32]

These uncertainties prompted us to perform a comprehensive analysis of the chemical structure and physicochemical properties of HA materials containing varying zinc concentrations. Our research employed a range of analytical techniques, including transmission electron microscopy (TEM), powder X-ray diffraction (PXRD), Fourier transform infrared (FT-IR) and Raman spectroscopy, flame atomic absorption spectrometry (F-AAS), and solid-state nuclear magnetic resonance (ssNMR) spectroscopy. In addition, the preliminary biological tests were performed.

Materials and Methods

Synthesis

Pure, unsubstituted HA and eight different zinc-substituted HA with Zn/(Zn+Ca) molar ratios ranging from 0.1 to 1.8 mol % were synthesized using the most commonly employed wet-chemical method.[32] The synthesis utilized widely used reagents as sources of calcium, zinc, and phosphorus: calcium nitrate tetrahydrate $Ca(NO_3)_2{\cdot}4H_2O$, zinc nitrate hexahydrate $Zn(NO_3)_2{\cdot}6H_2O$, and ammonium dihydrogen phosphate $(NH_4)_2HPO_4$. These substances were carefully weighed for each synthesis to maintain a (Ca+Zn)/P molar ratio of 1.67, corresponding to the molar ratio in stoichiometric HA. The synthesis was conducted at room temperature under ambient air conditions. A 100 mL solution of ammonium dihydrogen phosphate was added dropwise to a 400 mL solution previously prepared with calcium and zinc ions. The resulting suspension was continuously stirred during the addition, and the pH was adjusted to 9.5 using concentrated ammonia. The reaction equation is as follows:

$$(10 - \mathrm{x})\mathrm{Ca}^{2+} + \mathrm{x}\,\mathrm{Zn}^{2+} + 6\,\mathrm{PO_4}^{2-} + 2\,\mathrm{OH}^- \rightarrow \mathrm{Ca}_{10-\mathrm{x}}\mathrm{Zn}_{\mathrm{x}}(\mathrm{PO_4})_6(\mathrm{OH})_2$$

After two hours of stirring, the precipitate was left in the mother solution and subjected to an ageing process for three days. The precipitate was then centrifuged and repeatedly washed with distilled water to remove residual ammonia and soluble reaction by-products. The obtained material was dried at 100°C for 24 hours. Subsequently, the dried powder was micronized using a mortar and subjected to physicochemical analysis.

Physicochemical Analysis

The morphology of the synthesized crystals was examined using TEM at a voltage of 80 kV (JEM 1400, Jeol Co., Japan). Before measurement, the samples were suspended in anhydrous ethanol and drop-cast onto a Formvar-coated grid. The images were taken using a high-resolution digital camera (CCD MORADA, SiS Olympus, Germany). Elemental analysis was performed using an energy-dispersive X-ray spectroscopy (EDS) system (INCA Energy TEM, Oxford Instruments, UK) integrated with the microscope.

The zinc content in the obtained powders was also determined by F-AAS (AAnalyst PerkinElmer). Three samples of each powder were dissolved in pure 65% nitric acid (HNO_3) and then diluted properly to the appropriate volume with deionized water. All the measurements were performed in triplicate, according to the five-point standard curve ($y = 0.3621x + 0.0037$; coefficient of determination $R^2 = 0.9996$; linear range: 0.06–0.75 ppm). The relative standard deviation (%RSD) for triplicate measurements of each sample ranged from 0.1% to 1.8%. The highest RSD (1.8%) was observed for the lowest Zn content sample (0.1 mol%), while for all other samples %RSD did not exceed 1.1%.

Powder X-ray diffraction (PXRD) was employed to perform phase identification of the synthesized samples. Measurements were done using a Bruker D8 Discover diffractometer (Bruker, Madison, WI, US). Diffraction patterns were collected over a 2θ range of 10° to 60°, utilizing Cu Kα radiation (λ = 1.54056 Å, 40 mA, 40 kV), with a step increment of 0.03. The Bragg-Brentano geometry was used. Crystalline phase detected in the diffractograms was identified by comparison with the standard pattern (JCPDS-9-0432). The average crystallite size of the apatite phase was determined using the Scherrer equation as follows:

$$d = \frac{0.94\lambda}{\beta \cos\theta} \tag{1}$$

where

d – crystallite size (nm)

λ – radiation wavelength (nm)

β – the line full width at half maximum intensity (radians)

θ – the diffraction angle of the corresponding reflex (°).

The (002) and (300) reflections were chosen to calculate the crystallite sizes of the samples. We repeated the peak fitting procedure three times to estimate the measurement error associated with the determination of β from PXRD patterns. The variation between these independent refinements was minimal, and the resulting error in the crystallinity calculation did not exceed 0.8%.

The *a* and *c* crystal lattice parameters were determined using Topas software (Bruker, Germany). The error of the measurements did not exceed 0.3%. To estimate the crystallinity of the samples, the crystallinity index (CI) was calculated using the following formula:[33]

$$CI_1 = \left(0.24/\beta_{(002)}\right)^3, \tag{2}$$

where

CI_1 - crystallinity index

β – the line (002) full width at half maximum intensity (radians).

FT-IR spectroscopy experiments in the mid-range (4000–400 cm^{-1}) were carried out using a Spectrum 1000 spectrometer (PerkinElmer, Llantrisant, UK) with transmission mode and KBr pellets at room temperature. The spectra were recorded with a resolution of 2 cm^{-1} and 30 scans.

All the FT-IR spectra were processed with the GRAMS/AI 8.0 software (Thermo Scientific), which was also used for integration, deconvolution, differentiation and curve fitting of overlapping bands (υ_4 and υ_{1+3} regions). FT-IR spectra were used to determine the content of carbonate ions with the method described by Clasen and Ruyter.[34]

The Raman spectroscopy measurements were performed using an iRaman Plus 785S (B&W Tek, Newark, DE, USA) spectrometer. The conditions were as follows: 20× lens magnification, 500 repetitions of 1000 ms and 100% laser power, with a laser wavelength excitation of 785 nm. The spectra were recorded from 200 to 4000 cm^{-1} at room temperature.

All the NMR experiments were carried out on a NMR Avance III HD 600 MHz spectrometer (Bruker, Germany) with 3.2 mm rotors, magic angle spinning (MAS) at 23 kHz for ^1H and 7 kHz for ^{31}P experiments. Chemical shifts were referenced to tetramethylsilane (TMS) and 85% H_3PO_4 for protons and phosphorus-31 nuclei, respectively. ^1H MAS NMR spectra were recorded using a single pulse sequence (Bloch-decay, BD), 32 scans and with a 10s recycle delay. ^{31}P MAS NMR experiments were performed using a single-pulse sequence (32 scans, 10s recycle delay) and a $^1H \rightarrow ^{31}P$ cross-polarization (CP) sequence (contact time = 2 ms; recycle delay = 10s).

The release of zinc ions from the samples was assessed using 50 mL Falcon tubes filled with distilled water. In brief, three samples of each powder (0.500 ± 0.001 g) were enclosed in dialysis membranes, submerged in 50 mL of release medium, and agitated in a bath shaker at 100 rpm and 37 °C. The incubation lasted for 49 days.

At predetermined intervals (1 hour, 8 hours, 24 hours, 7 days, 14 days, 21 days, 28, 35, and 49 days), 10 mL samples were collected. The withdrawn amount was replaced with fresh distilled water to maintain volume consistency.

Zinc ion concentrations were measured using F-AAS on an AAnalyst 400 AA Spectrometer (Perkin Elmer, Waltham, MA, USA), detecting at a wavelength of 213.86 nm. Calibration curves were established using zinc ion standards ranging from 0.06 to 0.75 mg/mL (prepared by diluting a standard solution 1000 ppm). Each sample was measured in triplicate to ensure accuracy.

In vitro Cytotoxicity Assessment

The cytotoxic potential of the investigated materials was evaluated in vitro using two complementary assays: the Neutral Red Uptake (NRU) assay and the tetrazolium salt reduction assay (MTT). Both tests were conducted employing the BALB/c 3T3 clone A31 cell line (mouse embryonic fibroblasts; ATCC), a widely accepted model for biocompatibility testing.

In the NRU assay, cell viability was determined based on the ability of viable cells to incorporate and retain the supravital dye neutral red within lysosomes, whereas non-viable cells lack this capacity. The assay was performed in accordance with the ISO 10993–1:2009 guidelines,[35] and the absorbance of extracted dye was measured spectrophotometrically at 540 nm using an Asys UVM340 Hightech microplate reader.

The MTT assay was carried out by exposing the cells to material extracts, followed by incubation with the tetrazolium salt MTT (3-(4,5-dimethylthiazol-2-yl)-2,5-diphenyltetrazolium bromide). Viable cells reduce MTT to insoluble formazan crystals, which were subsequently solubilized and quantified by absorbance measurement at 560 nm. This procedure adhered to the ISO 10993–5:2009 standard protocol.[35]

Sample extracts were prepared by incubating 50 mg/mL of the tested material in culture medium for 24 hours at 37°C with gentle agitation, followed by sterile filtration. Polyethylene film (non-cytotoxic control) and latex (cytotoxic control) were employed as reference materials. Cell viability was expressed as a percentage relative to untreated control cells, and a viability threshold of 70% was used to define cytotoxicity. Samples were classified as non-cytotoxic if viability remained ≥70% across all tested dilutions. All assays were performed in triplicate ($n \geq 3$), and data are reported as mean values ± standard deviation (SD).

Results and Discussion

Zn^{2+} Content in the Materials – F-AAS Spectrometry

A series of zinc-enriched HAs (ranging from 0.0 to 11.2 wt% Zn^{2+}, corresponding to 0.0 to 1.8 mol%, calculated as the number of moles of Zn ions per 1 mole of HA) was synthesized via aqueous precipitation. This substitution's range was deliberate: it allowed us to capture progressive structural, spectroscopic, and morphological changes while remaining within the substitutional regime of hydroxyapatite. Literature reports indicate that at zinc concentrations of ~2.0 mol% or higher, secondary crystalline phases such as zinc phosphates readily form, potentially obscuring the intrinsic structure–property relationships of Zn-substituted hydroxyapatite. By restricting the substitution to below this threshold, we aimed to ensure phase purity of the HA lattice while still approaching the upper limit of zinc incorporation. For the synthesis, commonly used reagents were employed: calcium nitrate tetrahydrate, zinc nitrate hexahydrate, and ammonium dihydrogen phosphate, serving as sources of calcium, zinc, and phosphorus, respectively. The measured Zn content in the samples is presented in Table 1.

Table 1 Zn Content in the Obtained Materials

	Nominal Zn Content (mol%)	Nominal Zn Content (wt.%)	Experimental Zn Content (wt.%)	Efficacy of Substitution (%)
HA	–	–	–	–
0.1ZnHA	0.1	0.65	0.90 ± 0.16	139.1 ± 17.3
0.2ZnHA	0.2	1.30	1.22 ± 0.07	94.1 ± 5.7
0.4ZnHA	0.4	2.58	2.30 ± 0.07	89.0 ± 3.0
0.6ZnHA	0.6	3.85	3.61 ± 0.03	93.7 ± 0.8
0.8ZnHA	0.8	5.11	4.63 ± 0.12	90.7 ± 2.7
1.0ZnHA	1.0	6.35	5.59 ± 0.26	88.0 ± 4.7
1.4ZnHA	1.4	8.81	8.20 ± 0.21	93.1 ± 2.7
1.8ZnHA	1.8	11.20	9.47 ± 0.01	84.5 ± 0.1

The obtained results indicate that Zn^{2+} ions are readily incorporated into the HA lattice within the studied range, with substitution efficiencies ranging from 84.5±0.1% to 139.1±17.3%. This behavior can be attributed to the identical valence of calcium and zinc cations, as well as the smaller ionic radius of Zn^{2+} (74 pm) compared to Ca^2+ (99 pm). Although Mg^2+ ions have a comparable ionic radius (72 pm), they substitute much less efficiently (approximately 0.5%), suggesting that ionic radius and charge alone do not determine substitution behavior.[36] It can therefore be assumed that Zn^{2+} ions exhibit better geometric compatibility, more favorable coordination preferences, and stronger bonding with phosphate groups. Calcium ions (Ca^2+) may be approximately regarded as central ions in coordination complexes, occupying specific positions surrounded by oxygen atoms from phosphate (PO_4^{3-}) and hydroxyl (OH^-) groups. In the HA lattice, Ca(I) ions are located in seven-coordinated positions, while Ca(II) ions occupy nine-coordinated ones. Zn^{2+} ions prefer six- or sevenfold coordination, which makes them more compatible with the calcium sites in HA.[37,38] It can therefore be suspected that Zn^{2+} ions are preferentially introduced into the Ca(I) position. Previous experimental and computational work indicates that Zn^{2+} preferentially replaces Ca(I), due to its geometry and fewer ligands.[26,39] However, there were also studies showing the Ca(II) position as energetically and geometrically more desirable.[27] In contrast, Mg^{2+} ions favor sixfold (octahedral) coordination, which is less compatible with the geometry of HA. Furthermore, Zn^{2+} forms stronger bonds with PO_4^{3-} groups than Mg^{2+}, which supports structural stabilization at higher substitution levels.

The substitution efficiency of zinc in the 0.1ZnHA sample exceeded 100% (131.1 ± 17.3%), which may appear surprising; however, it should be noted that zinc ions tend to adsorb onto the HA surface, particularly at low concentrations.[40] This may result in an increased Zn^{2+} content detected in the analysis, even though not all ions are incorporated into the crystalline structure of the apatite. To complement the quantitative measurements obtained by FAAS and to gain insight into the localization of Zn-containing phases, TEM-EDS analysis was performed on selected samples. The EDS method provides information on the elemental distribution at the morphological level. Results are presented in Table 1s and Figure 1s in Supplementary Materials. EDS measurements were performed at six randomly selected points on the sample surface. The spectra revealed comparable zinc signals across the analyzed areas, indicating a relatively uniform distribution of zinc in the material, with some natural local variability.

Ultrastructure and Crystallinity – Transmission Electron Microscopy and Powder X-Ray Diffractometry

Figure 1 presents electron microscopy images of all synthesized powders. The sample of pure, unsubstituted HA consists of elongated nanocrystals with considerable size inhomogeneity, typical for HA synthesized by the precipitation method.[41]

As the Zn^{2+} ion content increases, the crystallites gradually lose their needle-like morphology and become more plate-like. Additionally, their size decreases significantly with increasing Zn^2+ content up to 0.8 mol%. The 0.8ZnHA sample exhibits the smallest crystallites and the strongest tendency to form agglomerates. Notably, in samples with higher Zn content, in addition to fine crystallites, spherical grains of amorphous nature are observed. The number and diameter of these grains increase with

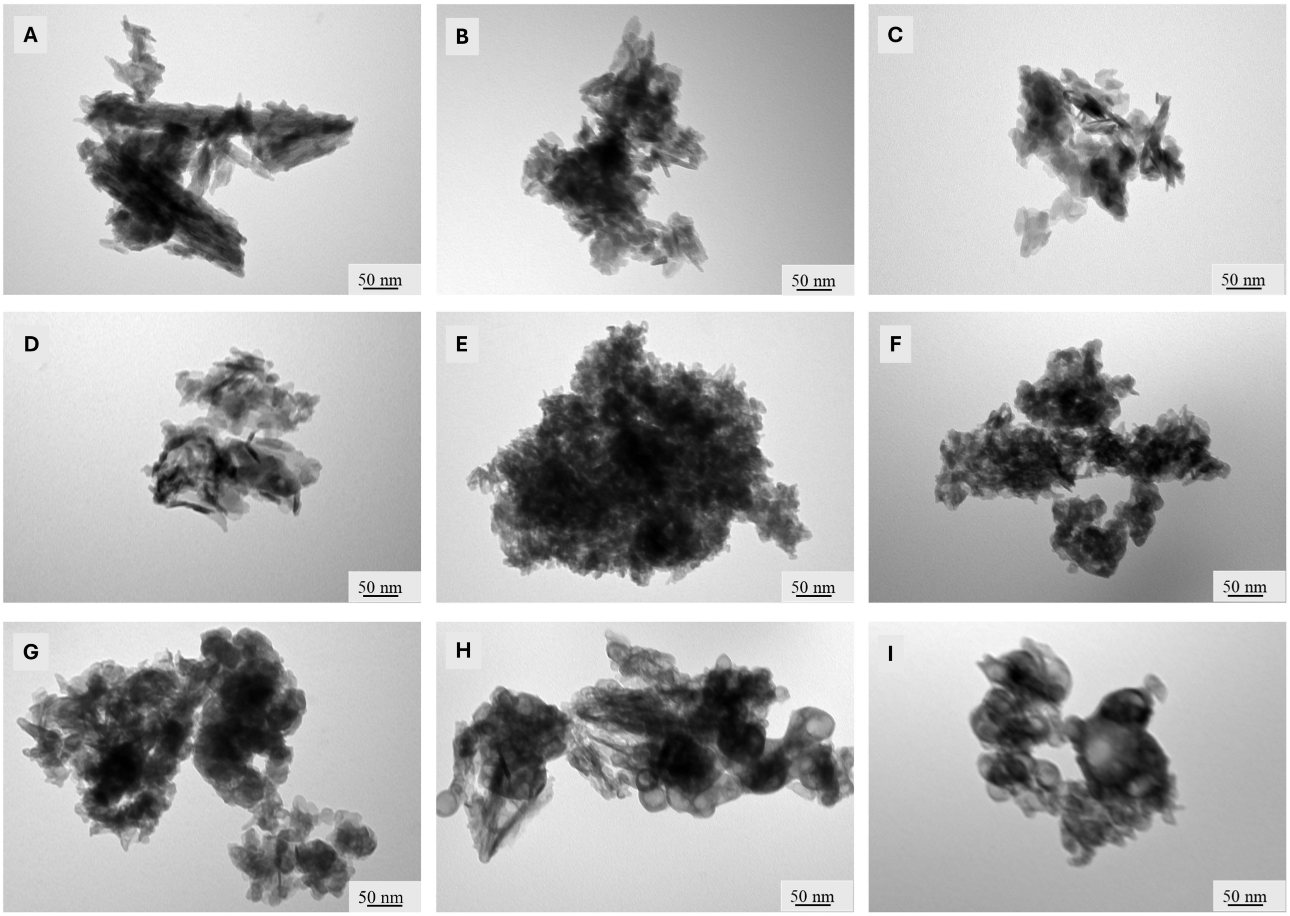

Figure 1 Transmission electron microscopy (TEM) micrographs of the obtained samples: HA (**A**); 0.1ZnHA (**B**); 0.2ZnHA (**C**); 0.4ZnHA (**D**); 0.6ZnHA (**E**); 0.8ZnHA (**F**); 1.0ZnHA (**G**); 1.4ZnHA (**H**); 1.8ZnHA (**I**).

increasing Zn content. Similar to the crystallites, the amorphous grain clusters are densely packed, forming a cohesive structure.

Figure 2 presents the PXRD diffractograms of all samples. Regardless of the Zn content, all reflections can be attributed exclusively to the crystalline structure of HA (JCPDS-09–0432). Thus, the samples do not contain crystalline impurities, which is consistent with previous studies where the introduction of Zn above 2.0 mol% resulted in the formation of additional phases such as $Ca_2Zn(PO_4)_3{\cdot}2H_2O$, $CaZn_2(PO_4)_3{\cdot}2H_2O$, and $Zn_3(PO_4)_3{\cdot}2H_2O$.[25,42] However, increasing Zn content results in noticeable broadening of the diffraction peaks and a decrease in peak separation, further corroborating previous findings.[43] The diffractogram of the 1.8ZnHA sample is significantly broadened with poorly defined reflections, indicating a low degree of crystallinity and/or the formation of an amorphous phase, which is consistent with TEM observations.

The calculated crystallite sizes, crystallinity values, and unit cell parameters of the obtained materials are presented in Table 2. The *c* parameter decreases with increasing Zn content, indicating a shortening of the unit cell along the *c*-axis. The *a* parameter also changes, but no clear trend can be identified. Interestingly, the *a* value for the 1.8ZnHA sample is similar to that of pure HA. Previous investigations into the influence of zinc ion substitution on unit cell parameters have yielded inconsistent results. Theoretical studies indicated a reduction in both *a* and *c* lattice constants.[27,44] In contrast, experimental work by Li et al[45] and Shepherd et al[46] reported an increase in the *c* parameter accompanied by a decrease in *a*, suggesting a preferential substitution of Zn^{2+} ions at the Ca(II) sites. Our findings align with those of Webster et al.[47] Mijaji et al[23] and Ren et al[22] who clearly demonstrated a decrease in the *c* parameter with increasing concentrations of substituted zinc ions. The irregularity of the a parameter may arise from overlapping effects, including occupation of both Ca(I) and Ca(II) sites at higher substitution levels,

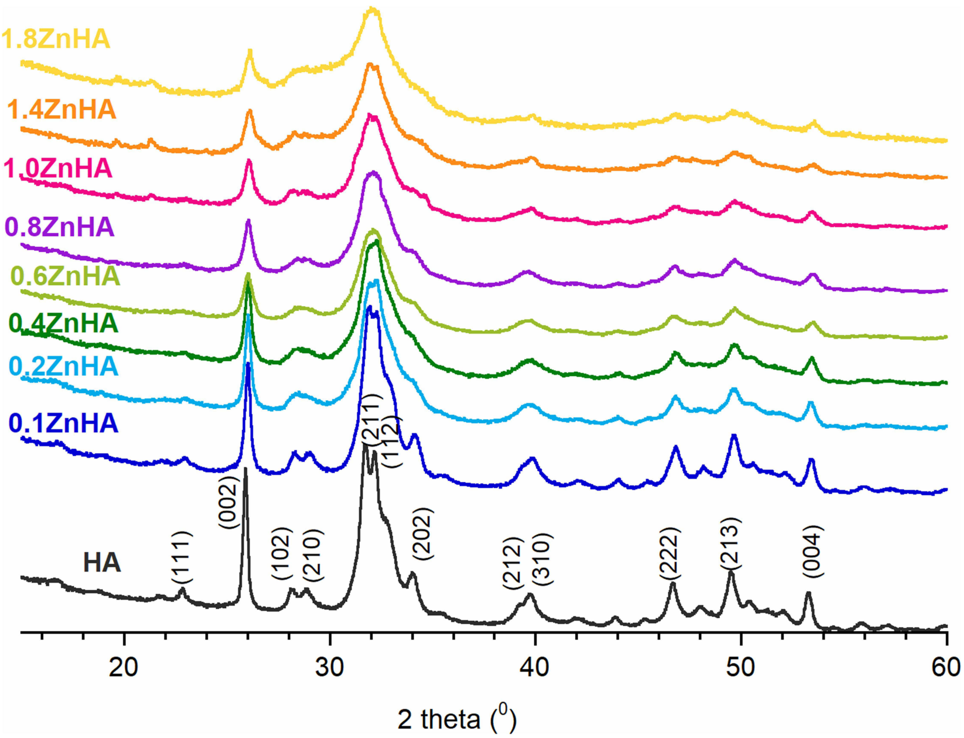

Figure 2 Powder X-ray diffractometry (PXRD) patterns of the obtained samples.

local lattice distortions, partial amorphization, and the growing influence of the hydrated surface layer in Zn-rich samples (a more detailed discussion of this aspect is provided later in the Results and Discussion). Together, these factors suggest that Zn substitution modifies HA not only through direct ionic replacement but also via induced disorder and local environmental changes, complicating the interpretation of unit cell.

Crystallite sizes along the *a* and *c* axes were calculated using the Scherrer equation (Table 2). As confirmed by TEM experimental data, the samples contain elongated nanocrystals at low Zn content, which become significantly smaller and more plate-like with increasing Zn substitution, particularly along the *c*-axis.

The results (see Table 2) demonstrate a decreasing trend in HA crystallinity with increasing Zn content, consistent with previously reported literature.[22] The crystallinity index was also calculated using the obtained FT-IR spectra by the method described in.[48] The results (see Table 2) showed a similar trend of significant decrease in crystallinity with increasing amount of Zn^{2+} introduced into HA.

Table 2 Various Crystallographic Parameters of the Obtained Samples

	a (Å)[a]	c (Å)[a]	Crystallinity Index[b]	Crystallinity Index[c]	Crystal sizes[d] Along c and *a* Axes (nm)
HA	9.4260	6.8804	0.955	0.195	35/8
0.1ZnHA	9.4056	6.8502	0.411	0.152	27/8
0.2ZnHA	9.4410	6.8467	0.327	0.186	24/6
0.4ZnHA	9.4365	6.8459	0.261	0.169	23/6
0.6ZnHA	9.4627	6.8462	0.0998	0.127	16/6
0.8ZnHA	9.4614	6.8426	0.110	0.101	18/6
1.0ZnHA	9.4639	6.8344	0.105	0.0754	17/7
1.4ZnHA	9.4131	6.8243	0.0885	0.0496	16/6
1.8ZnHA	9.4240	6.8218	0.0915	0.0296	16/4

Notes: [a]Error ± 0.3% [b]measured from PXRD patterns, according to [33]. [c]measured from FTIR spectra, according to [49]. [d]calculated according to Scherrer's formula and using (002) and (310) reflections.

https://doi.org/10.2147/NSA.S545378

Chemical Structure and Composition – FT-IR and Raman Spectroscopies, ^{1}H and ^{31}P Solid-State NMR Spectroscopy

Figure 3 presents representative FT-IR spectra showing typical HA bands. The dominant bands are located in the 1200–900 and 600–500 cm^{-1} regions, corresponding to ν_{1+3} and ν_4 phosphate vibrations, respectively.[49] The curve fitting results for both spectral regions are presented in Figures 2s and 3s and in Tables 2s and 3s, respectively.

Stretching and libration bands of structural hydroxyl groups are normally observed at 3570 and 630 cm^{-1}, respectively. These bands are very weak in the spectra of pure HA and the samples with up to 0.6 mol% Zn^{2+}, and become undetectable at higher Zn contents (0.8–1.8 mol%). The curve fitting of the 650–500 cm^{-1} region reveals the OH librational band in the spectra of all the samples; however, its relative intensity decreases significantly (see Table 2s and Figure 2s in Supplementary Materials).[50,51] A similar trend is observed in the ^{1}H BD NMR spectrum (Figure 4A), where the signal at approximately 0 ppm corresponds to structural OH protons aligned along the *c*-axis and significantly decreases with increasing Zn content (Table 4s and Figure 4s in Supplementary Materials). Using the method described in,[52] the relative content of structural OH groups was calculated (Figure 4B), ranging from 94% to 8% compared to stoichiometric HA.

This dramatic decrease in the content of structural hydroxyl groups may have various causes. One of them is the potential location of Zn ions in the OH columns and disrupting their ordering, according to the reaction:

$$Ca_{10}(PO_4)_6(OH)_2 + x\,Zn^{2+} \rightarrow Zn_xCa_{10}(PO_4)_6O_2 + 2x\,H^+$$

Zn^{2+} ions can also be inserted through non-substitutional mechanisms, as reported in the literature.[53] Another contributing factor may be the increasing disorder in and around the *c*-axis channels, which can accommodate water molecules. In stoichiometric HA, OH groups are spaced 3.44 Å apart, too far to form hydrogen bonds. Pajchel et al[54] reported that water molecules adsorbed on the HA surface may migrate into the crystal lattice, facilitated by proton transfer involving water and hydroxide ions in the *c*-axis channels. There is also likely a physical diffusion of water molecules to fill empty spaces in the *c*-axis channels. Another possible reason is the increased contribution of the hydrated surface layer of hydroxyapatite crystals.[54,55] Taken together, these scenarios represent plausible explanations rather than definitive

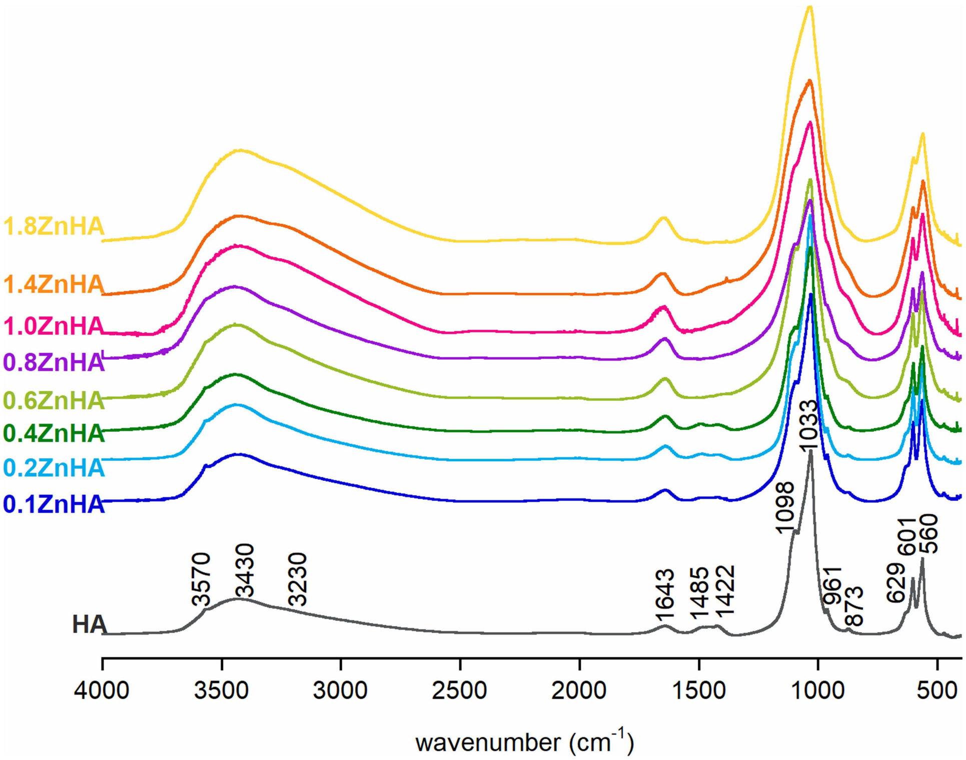

Figure 3 Fourier transform infrared (FT-IR) spectra of the obtained samples.

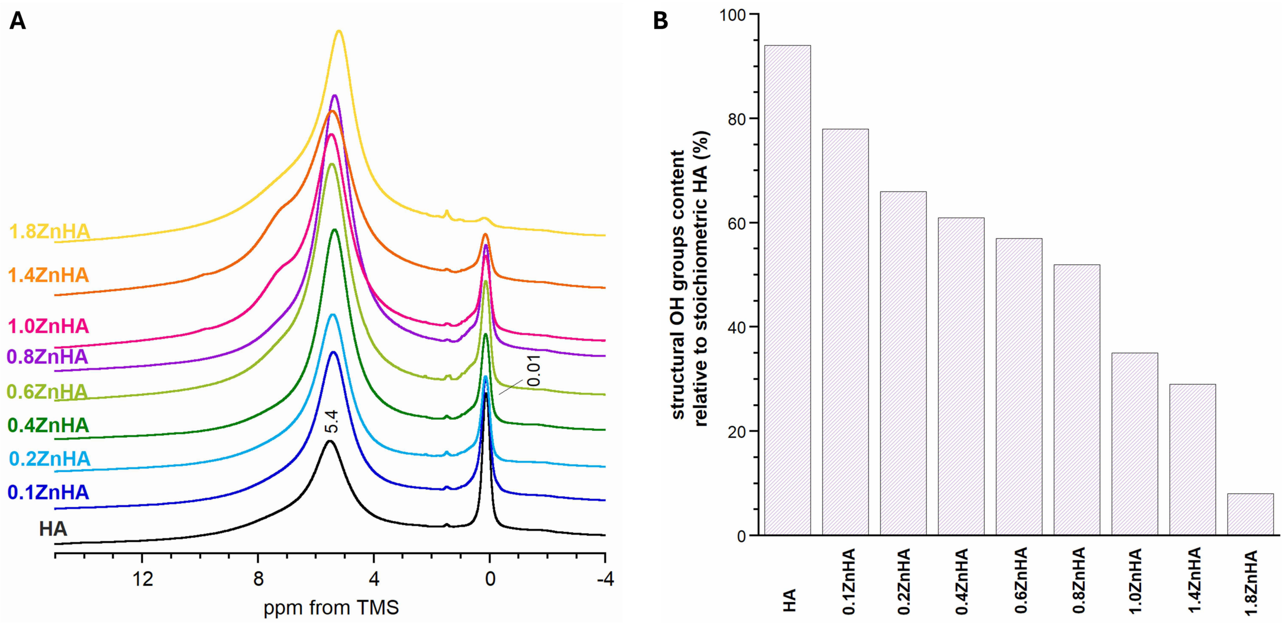

Figure 4 ^{1}H Bloch-decay (BD) magic-angle spinning (MAS) NMR spectra of the obtained samples (**A**). Structural OH groups content relative to stoichiometric HA (%) calculated from proton ssNMR spectra (**B**).

mechanisms, and further studies employing advanced structural and spectroscopic methods will be required to unambiguously determine the origin of the OH$^-$ depletion.

According to the literature,[55] HA nanocrystals, in addition to a typical crystalline core, have a semi-liquid surface layer that contains not only adsorbed water molecules but also a variety of ions: calcium, phosphates, carbonates, acidic phosphates, and, in the case of substituted hydroxyapatites, cations and anions (in our case, zinc ions) may adsorb there. The presence of this hydrated surface layer was further confirmed by^{31} P (cross-polarization CP and Bloch-decay BD) NMR experiments (Figure 5A and B and Figure 5s in Supplementary Materials). Both spectra reveal a broad signal at approximately 3.7 ppm attributed to 31-phosphorus nuclei in a water-rich environment and a narrow signal (at

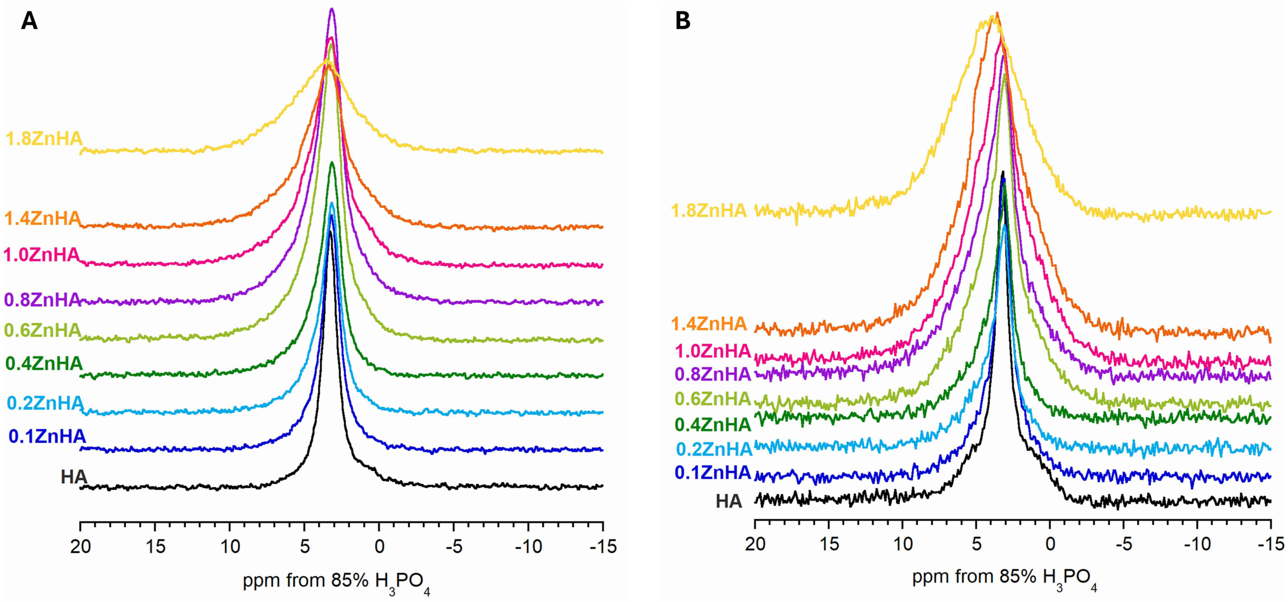

Figure 5 ^{31}P Bloch-decay (BD) magic-angle spinning (MAS) NMR (**A**) and ^{31}P cross-polarization (CP) MAS NMR (**B**) spectra of the obtained samples.

https://doi.org/10.2147/NSA.S545378

approximately 3.1 ppm) corresponding to 31-phosphorus sites close to the structural OH groups.[54] The water-rich environment is primarily associated with the surface hydrated layer of HA crystals and may also be related to disordered intracrystalline regions containing water molecules (structural water). Thus, the broad component represents the signals from phosphorus-31 nuclei located mainly in the hydrated surface water region (and in the ^{31}P CP experiment, cross-polarizing from protons of water). In turn, the narrow signal at 3.1 ppm originates from phosphorus-31 nuclei located in the crystal interior (and in the ^{31}P CP NMR experiment, cross-polarizing from protons from structural OH groups).

Our experimental data clearly show that the broad signal increases with Zn content (Figure 5s, Table 5s and Supplementary Materials), supporting the growing contribution of the hydrated surface layer.

FT-IR and ^{1}H NMR spectra also confirm the presence of this layer. In FT-IR spectra, a broad band at ~3430 cm^{-1} and a weaker band at 1640 cm^{-1} correspond to the stretching and bending vibrations of water OH groups, respectively. In ^{1}H NMR, a broad signal at 5.4 ppm corresponds to water protons.[56,57] Both techniques show increasing relative intensity of these bands with increasing Zn content, indicating greater water adsorption. Although direct imaging of this layer by HR-TEM was not available in the present study, complementary analyses such as TGA (to quantify water content) and HR-TEM (to visualize the layer morphology) are planned for future work to provide further structural and quantitative insights.

Regarding common impurities in HA obtained by wet precipitation, hydrogen phosphate ions (HPO_4^{2-}) are usually detectable In ^{1}H NMR, acidic phosphate groups (as in brushite) typically give a signal at approximately 10.4 ppm.[58] In both HA and Zn-substituted samples, this signal is not observed, indicating the absence of brushite-derived HPO_4^{2-} (see Figures 4A and 4s in Supplementary Materials). This is supported by the absence of a 1.3 ppm signal in ^{31}P NMR (see Figure 5A and B and 5s in Supplementary Materials).[58] However, a 7.8 ppm signal appears in the ^{1}H NMR spectra of samples with >0.6 mol% Zn, possibly originating from P–OH groups on crystal surfaces (Table 4s in Supplementary Materials). Its proximity to the water signal (5.4 ppm) and decreasing intensity in the 1.8ZnHA sample suggest a surface-localized origin. FT-IR also supports this data: relative intensity of bands at 540 cm^{-1} (ν_4 region) and 1145 cm^{-1} (ν_{1+3}) increases with Zn content, except for 1.8ZnHA, aligning with ^{1}H NMR results (see Figure 2s, 3s and Tables 2s, 4s in Supplementary Materials).[59,60]

FT-IR spectra (Figure 2) indicate the presence of carbonate bands (1500–1400 cm^{-1} and 890–860 cm^{-1}) exclusively in the samples of unsubstituted HA and HA substituted with a small amount of Zn^{2+} (up to 0.4 mol%).[60] The position of these bands suggests that they are primarily B-type carbonates, and their content, estimated using the method proposed by Clasen and Ruyter,[34] ranges from 0.22 wt.% for HA to 0.15 wt.% for 0.4ZnHA. For samples with a high Zn^{2+} content, the carbonate bands are absent, which may suggest that carbonates compete with Zn^{2+} ions in the crystal structure, making their simultaneous incorporation energetically unfavorable. Our observations that carbonate bands diminish with increasing Zn content are consistent with previous studies reporting that Zn incorporation alters crystal growth and lattice environments, thereby limiting carbonate incorporation in HA. The effect likely arises from a combination of (i) Zn-induced lattice distortions (altered Ca sites), (ii) reduced crystallinity and enhanced hydrated surface layers that change surface adsorption behaviour, and (iii) the possible formation of Zn-rich amorphous surface phases that compete with carbonate for incorporation/adsorption sites. These mechanisms have been reported in similar Zn-carbonate HA systems.[29,32,61]

Raman spectra were also recorded for all obtained samples (see Figure 6). The spectra are dominated by a band at approximately 959 cm^{-1}, which originates from the ν_1 PO_4 vibrations. The band at around 1046 cm^{-1}, corresponding to the ν_3 vibrations, is characterized by relatively low intensity, which is consistent with previous literature reports.[62,63]

Particular attention should be paid to the spectra of the 1.0ZnHA, 1.4ZnHA, and 1.8ZnHA samples, where two additional bands are observed: at 999 cm^{-1} and 550 cm^{-1} (their intensity increases with the amount of zinc introduced). These bands can be attributed to the vibrations of phosphate groups in amorphous zinc phosphate,[64] which would support the results obtained by PXRD and TEM methods.

Zn^{2+} Release Experiments

For the selected four materials (0.1ZnHA, 0.6ZnHA, 1.0ZnHA, and 1.8ZnHA), a Zn^{2+} ion release experiment was conducted over 7 weeks (49 days). Significantly, Zn^{2+} ion release was exceptionally low for all samples, with the cumulative Zn^{2+} content not exceeding 1%. For the 0.1ZnHA sample, concentrations were below the detection limit; therefore, the graph presents curves only for the 0.6ZnHA, 1.0ZnHA, and 1.8ZnHA samples (Figure 7).

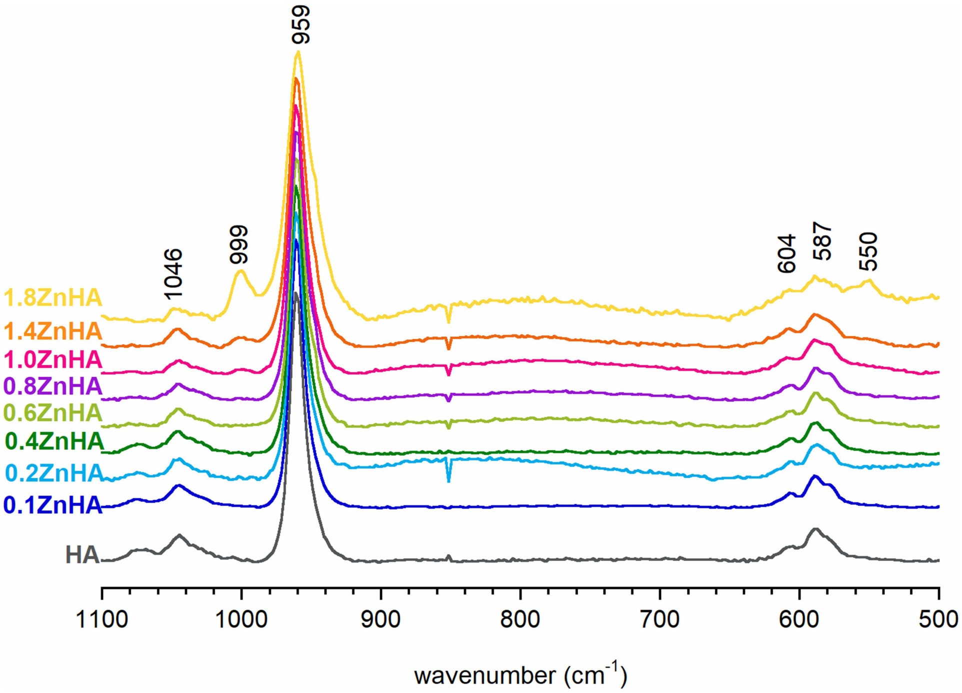

Figure 6 Raman spectra of the obtained samples.

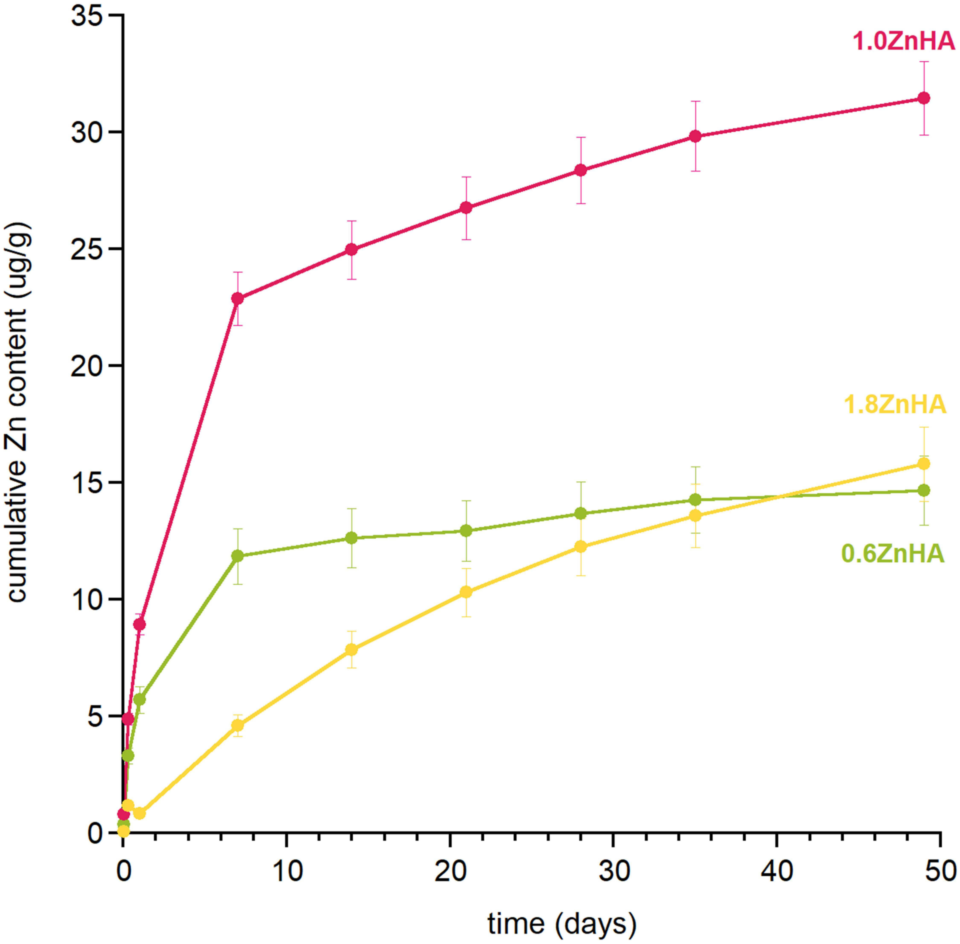

Figure 7 Zn^{2+} ions release from the selected samples.

https://doi.org/10.2147/NSA.S545378

The release profiles for the 0.6ZnHA and 1.0ZnHA samples are similar and are characterized by two phases. In the first phase (lasting up to 7 days), there is an intensive release of Zn^{2+} ions into the medium, followed by a significant decrease in the release rate. The initial phase may be attributed to the release of Zn^{2+} ions from the hydrated surface layer, which is less ordered than the crystalline core.

According to ^{31}P NMR studies, the hydrated surface layer content is higher in the 1.0ZnHA sample than in the 0.6ZnHA sample, which may account for the significantly faster release of Zn^{2+} ions from the 1.0ZnHA sample during the first seven days. After this period, the release of Zn^{2+} ions is likely due to the gradual dissolution of the crystalline apatite core.

The 1.8ZnHA sample exhibits gradual, prolonged release without a pronounced "burst release" effect. Notably, the cumulative amount of Zn^{2+} ions released is lower than in the other tested samples; only after 40 days does it reach a value comparable to the 0.6ZnHA sample.

As evidenced by both TEM microscopy images and ^{31}P NMR spectra, the 1.8ZnHA sample is characterized by a very low degree of crystallinity, and the particles (grains) are large and densely packed in compact agglomerates. This may explain the very low level of Zn^{2+} ion release into the medium, even though according to ^{31}P NMR, the hydrated surface was the largest for the 1.8ZnHA sample (see Figure 4s and Table 4s in Supplementary Materials). The gradual release occurs from a nearly amorphous material, which accounts for the absence of a "burst release" effect.

It can be assumed that the "two-phase" release for 0.6ZnHA and 1.0ZnHA is due to the presence of both crystalline and amorphous fractions, while in 1.8ZnHA, the lack of the first burst is due to the presence of mainly amorphous fractions.

In summary, the obtained results indicate that the mechanism and intensity of Zn^{2+} ion release are strongly dependent on the material's microstructure and degree of crystallinity, rather than solely on its nominal zinc content.

Cytotoxicity Tests

In the final stage of the study, the cytotoxicity of all synthesized samples was assessed using the MTT and NRU assays (see Table 3).

The NRU results indicated that all materials exhibited non-cytotoxic behavior, whereas in the MTT, two samples, 1.0ZnHA and 1.8ZnHA, were cytotoxic. The differences in results between the NRU and MTT assays may be due to different mechanisms. The NRU assay measures the ability of living cells to absorb and retain neutral red dye, reflecting cell membrane integrity and lysosomal activity. The MTT assay assesses mitochondrial enzymatic activity through the reduction of MTT to formazan by mitochondrial dehydrogenases, an indicator of cell viability. The higher toxicity of samples shown by the MTT test may be due to the effect of zinc ions on mitochondria. Zinc can interfere with mitochondrial function, leading to loss of membrane potential, reduced ATP production, and generation of reactive

Table 3 Cytotoxicity Results

Sample	NRU Test-Cells Viability ± SD[b] (%) 50mg/mL	MTT Test-Cells Viability ± SD (%) 50mg/mL	Classification
HA	98 ± 5	89± 4	Non-cytotoxic
0.1ZnHA	103 ± 2	77 ± 8	Non-cytotoxic
0.2ZnHA	91 ± 1	98 ± 28	Non-cytotoxic
0.4ZnHA	88 ± 12	97 ± 6	Non-cytotoxic
0.6ZnHA	93 ± 13	93 ± 4	Non-cytotoxic
0.8ZnHA	84 ± 4	93 ± 7	Non-cytotoxic
1.0ZnHA	112 ± 5	51 ± 16	Cytotoxic
1.4ZnHA	85 ± 11	91 ± 3	Non-cytotoxic
1.8ZnHA	97 ± 1	61 ± 11	Cytotoxic
PE[a]	86 ± 7	99 ± 7	Non-cytotoxic

Notes: [a]PE—polyethylene film, reference non-cytotoxic material. [b]SD—standard deviation. A decrease in the cell viability below 70% classifies the sample as cytotoxic.

oxygen species (ROS).[65–67] These mechanisms may lead to the increased cytotoxicity seen in the MTT assay compared to the NRU assay, which does not directly assess mitochondrial function.

Consequently, further investigations, including additional synthesis and characterization, are warranted to elucidate the underlying cause of the observed cytotoxicity in these particular samples.

Conclusions

The presented study provides a detailed analysis of how gradual substitution of calcium ions with zinc ions influences the physicochemical properties and biological behavior of HA. The results confirm that Zn^{2+} ions can be effectively incorporated into the HA lattice via aqueous precipitation, and their presence substantially influences the material's structural organization.

It was shown that increasing Zn^{2+} content leads to a progressive crystallinity decrease, crystal morphology transformation from needle-like to plate-like, and formation of amorphous phases. Simultaneously, spectroscopic analyses (FT-IR, Raman, NMR) revealed a significant disruption of the structural OH^{-} groups and an increase in the hydrated surface layer, which appears to play a central role in ion release and potential bioactivity. The substitution also limits carbonate incorporation, suggesting competitive interactions at the crystal surface or within the lattice.

Although the Zn^{2+} release from the materials was generally low, cytotoxic effects observed in MTT assays for samples with higher zinc content suggest that factors other than zinc ion release, such as structural characteristics or surface-related properties, may contribute to the observed cellular responses. The MTT assay measures mitochondrial enzyme activity, which can be affected by multiple cellular and material-related factors beyond ion release. Therefore, further in-depth investigations are required to elucidate the precise mechanisms underlying the observed cytotoxicity. This highlights the complexity of designing Zn-substituted HA materials for biomedical applications.

While Zn^{2+}-substituted hydroxyapatite has been the subject of numerous investigations, the present study provides a systematic and comprehensive physicochemical characterization across a wide substitution range. By combining complementary techniques (PXRD, FTIR, Raman, NMR, TEM, F-AAS), we consistently correlated reduction in crystallinity, structural OH^{-} depletion, and amorphous phase formation with zinc content. This integrated approach highlights how subtle structural modifications directly influence ion release behavior and cytotoxic responses, thus offering a more complete structure–property picture than is typically available.

Overall, the results highlight that zinc substitution exerts both beneficial and limiting effects. While moderate levels can enhance structural diversity and introduce potential antimicrobial or osteogenic functions, excessive substitution may compromise crystallinity and biocompatibility. These findings are directly relevant to ongoing applications of Zn-HA in bone grafts, coatings for implants, and drug delivery systems, where balancing biofunctionality with safety is crucial. Further work should refine synthesis strategies and in vitro/in vivo testing to consolidate the identified 0.6 mol% threshold as a translational design parameter.

Highlights

- Aqueous precipitation was used to synthesize Zn^{2+}-enriched hydroxyapatites.
- Zn^{2+} incorporation reduced the crystal size and crystallinity of hydroxyapatite.
- High Zn^{2+} levels induced the formation of an amorphous zinc phosphate phase.
- Spectroscopic data revealed decreased structural OH^{-} and carbonate, and increased acidic phosphate content.
- Zn^{2+} was distributed in both the crystalline core and hydrated surface layer.
- Zinc ion release remained low over 7 weeks, regardless of initial Zn^{2+} content.
- Cytotoxicity assays showed good biocompatibility up to 0.6 mol% Zn^{2+} doping.

Acknowledgments

We would like to thank Metrohm Polska for lending us an iRaman Plus 785S spectrometer to use in our research.

Author Contributions

Conception: JK, RG, EB; Study design: JK, MB, ŁP, MW; Execution: ŁP, MB, MW, JK; Acquisition of data: JK, RG, EB; Analysis and interpretation: ŁP, JK, MB, MW; Writing: JK, ŁP, MW; Reviewing and editing: RG, EB, MB, ŁP; Funding acquisition: JK, RG. All authors made a significant contribution to the work reported, whether that is in the conception, study design, execution, acquisition of data, analysis and interpretation, or in all these areas; took part in drafting, revising or critically reviewing the article; gave final approval of the version to be published; have agreed on the journal to which the article has been submitted; and agree to be accountable for all aspects of the work.

Funding

Studies were supported by the Medical University of Warsaw and the Warsaw University of Technology under the collaborative grant "Integra WUM-PW" (no. WF6/INTEGRA.1.4/N/23).

Disclosure

The authors report no conflicts of interest in this work.

References

1. Mondal S, Park S, Choi J, et al. Hydroxyapatite: a journey from biomaterials to advanced functional materials. *Adv Coll Interf Sci*. 2023;321:103013. doi:10.1016/j.cis.2023.103013
2. Palmer LC, Newcomb CJ, Kaltz SR, Spoerke ED, Stupp SI. Biomimetic systems for hydroxyapatite mineralization inspired by bone and enamel. *Chem Rev*. 2008;108:4754–4783. doi:10.1021/cr8004422
3. Z LR, Ito A, Ishikawa K, et al. LeGeros J P. fundamentals of hydroxyapatite and related calcium phosphates. In: Deville S, editor. *Advanced Biomaterials: Fundamentals, Processing, and Applications*. New York: Wiley Publisher; 2009:19–52.
4. Haider A, Haider S, Han SS, Kang I-K. Recent advances in the synthesis, functionalization and biomedical applications of hydroxyapatite: a review. *RSC Adv*. 2017;7:7442–7458.
5. Kolmas J, Krukowski S, Laskus A, Jurkitewicz M. Synthetic hydroxyapatite in pharmaceutical applications. *Ceram Int*. 2016;42:2472–2487.
6. Limeback H, Enax J, Meyer F. Biomimetic hydroxyapatite and caries prevention: a systematic review and meta-analysis. *Can J Dent Hyg*. 2021;55 (3):148–159.
7. George SM, Nayak C, Singh I, Balani K. Multifunctional hydroxyapatite composites for orthopedic applications: a review. *ACS Biomater Sci Eng*. 2022;8:3162–3186. doi:10.1021/acsbiomaterials.2c00140
8. Liu W, Cheong N, He Z, Zhang T. Application of hydroxyapatite composites in bone tissue engineering: a review. *J Func Biomater*. 2025;16 (4):127. doi:10.3390/jfb16040127
9. Munir MU, Salman S, Ihsan A, Elsaman T. Synthesis, characterization, functionalization and bio-applications of hydroxyapatite nanomaterials: an overview. *Int J Nanomed*. 2022;17:1903–1925. doi:10.2147/IJN.S360670
10. Pasteris JD, Wopenka B, Valsami-Jones E. Bone and tooth mineralization: why apatite? *Elements*. 2008;4(97):–. doi:10.2113/GSELEMENTS.4.2.97
11. Wang B, Zhang Z, Pan H. Bone apatite nanocrystal: crystalline structure, chemical composition, and architecture. *Biomimetics*. 2023;8:90. doi:10.3390/biomimetics8010090
12. Ressler A, Žužić A, Ivanišević I, Kamboj N, Ivanković H. Ionic substituted hydroxyapatite for bone regeneration applications: a review. *Open Ceramics*. 2021;6:100122. doi:10.1016/j.oceram.2021.100122
13. Uskoković V. Ion-doped hydroxyapatite: an impasse or the road to follow? *Ceram Int*. 2020;46:11443–11465. doi:10.1016/j.ceramint.2020.02.001
14. Casarrubios L, Gómez-Cerezo N, Sánchez-Salcedo N, Feito MJ. Silicon substituted hydroxyapatite/VEGF scaffolds stimulate bone regeneration in osteoporotic sheep. *Acta Biomater*. 2020;101:544–553. doi:10.1016/j.actbio.2019.10.033
15. Pajor K, Michalicha A, Belcarz A, et al. Antibacterial and cytotoxicity evaluation of new hydroxyapatite-based granules containing silver or gallium ions with potential use as bone substitutes. *Int J Mol Sci*. 2022;23(13):7102. doi:10.3390/ijms23137102
16. Tuntun SM, Hossain MS, Uddin MN, et al. Crystallographic characterization and application of copper-doped hydroxyapatite as a biomaterial. *New J Chem*. 2023;47:2874–2885. doi:10.1039/D2NJ04130H
17. Bhatnagar D, Gautam S, Sonowal L, Bhinder SS, Ghosh S, Pati F. ACS Appl. *Bio Mater*. 2024;7:2272–2282.
18. Ran L, Liu L, Gao J, et al. Strontium-doped hydroxyapatite and its role in osteogenesis and angiogenesis. *Int J Dev Biol*. 2023;67(4):137–146. doi:10.1387/ijdb.230091lc
19. Molenda M, Kolmas J. The role of zinc in bone tissue health and regeneration- a review. *Biol Trace Elem Res*. 2023;201:5640–5651. doi:10.1007/s12011-023-03631-1
20. O'Connor JP, Kanjilal D, Teitelbaum M, Lin SS, Cottrell JA. Zinc as a therapeutic agent in bone regeneration. *Materials*. 2020;13(10):2211. doi:10.3390/ma13102211
21. Amin N, Clark CCT, Taghizadeh M, Djafarnejad S. Zinc supplements and bone health: the role of the RANKL-RANK axis as a therapeutic target. *J Trace Elem Med Biol*. 2020;57:126417.
22. Ren F, Xin R, Ge X, Leng Y. Characterization and structural analysis of zinc-substituted hydroxyapatites. *Acta Biomater*. 2009;5:3141–3149.
23. Mijaji F, Kono Y, Suyama Y. Formation and structure of zinc-substituted calcium hydroxyapatite. *Mater Res Bull*. 2005;40:209–220.
24. Mardziach CM, Ramesh S, Wahid AMF, et al. Effect of zinc ions on the structural characteristics of hydroxyapatite bioceramics. *Ceram Int*. 2020;46:13945–13952.

25. Ofudje EA, Adeogun AI, Idowu MA, Kareem SO. Synthesis and characterization of Zn-Doped hydroxyapatite: scaffold application, antibacterial and bioactivity studies. *Helyon*. 2019;e01716.
26. Uysal I, Yilmaz B, Evis Z. Zn-doped hydroxyapatite in biomedical applications. *J Aust Ceram Soc*. 2021;57:869–897.
27. Tang Y, Chappell C, Dove F, Reeder MT, Lee RJ. Zinc incorporation into hydroxyapatite. *Biomater*. 2009;30:2864–2872.
28. Ito A, Ojima K, Naito H, Ichinose N, Tateishi T. Preparation, solubility, and cytocompatibility of zinc-releasing calcium phosphate ceramics. *J Biomed Mater Res*. 2000;50:178–183.
29. Hu W, Ma J, Wang J, Zhang S. Fine structure study on low concentration zinc substituted hydroxyapatite nanoparticles. *Mater Eng Sci C*. 2012;32:2404–2410.
30. Bhattacharjee P, Begam H, Chanda A, Nandi SK. Animal trial on zinc doped hydroxyapatite: a case study. *J Asian Ceram Soc*. 2014;2:44–51.
31. Kazimierczak P, Golus J, Kolmas J, Wójcik M, Kolodyńska D, Przekora A. Noncytotoxic zinc-doped nanohydroxyapatite-based bone scaffolds with strong bactericidal, bacteriostatic, and antibiofilm activity. *Biomater Adv*. 2022;213011.
32. Dornelas J, Dornelas G, Rossi A, et al. The incorporation of zinc into hydroxyapatite and its influence on the cellular response to biomaterials: a systematic review. *J Funct Biomater*. 2024;15(7):178. doi:10.3390/jfb15070178
33. Sa Y, Guo Y, Feng X, et al. Are different crystallinity-index-calculating methods of hydroxyapatite efficient and consistent? *New J Chem*. 2017;41:5723–5731.
34. Clasen ABS, Ruyter I. Quantitative determination of type A and type B carbonate in human deciduous and permanent enamel by means of Fourier transform infrared spectrometry. *Adv Dent Res*. 1997;11(4):523–527.
35. I. O. for Standardization, 'ISO 10993-5: 2009-Biological evaluation of medical devices-Part 5: tests for in vitro cytotoxicity. *ISO Geneva*. 2009.
36. Bigi A, Falini G, Foresti E, Ripamonti A, Gazzano M, Roveri N. Magnesium influence on hydroxyapatite crystallization. *J Inorg Biochem*. 1993;49(1):69–78.
37. Shannon RD. Revised effective ionic radii and systematic studies of interatomic distances in halides and chalcogenides. *Acta Crystallographica*. 1976;32(5):751–767.
38. LeGeros RZ. Incorporation of Mg^2+ and Zn^2+ into the apatite lattice.Clin. *Orthop Relat Res*. 1988;223:226–235.
39. Boanini E, Gazzano M, Bigi A. Ionic substitutions in calcium phosphates synthesized at low temperature. *Acta Biomater*. 2010;6(6):1882–1894.
40. Pivarciova I, Rosskopfova O, Galambos M, Rajec P. Adsorption behavior of Zn(II) ions on synthetic hydroxyapatite. *Desalin Water Treat*. 2015;55:1825–1831.
41. Mohd Pu'ad NAS, Haq RHA, Mohd Noh H, Abdullah HZ, Idris MI, Lee TC. Synthesis method of hydroxyapatite: a review. *Mater Today Proc*. 2020;29:233–239.
42. Ijaz K, Khalid H, Chaudhry AA. Zinc-substituted hydroxyapatite. In: AA C, AS K editors. *Handbook of Ionic Substituted Hydroxyapatite. 2020*. 217–236. Woodhead Publishing Series in Biomaterials. Elsevier
43. Thian ES, Konishi T, Kawanobe Y, et al. Zinc-substituted hydroxyapatite: a biomaterial with enhanced bioactivity and antibacterial properties. *J Mater Sci Mater Med*. 2013;24(2):437–445. doi:10.1007/s10856-012-4817-x
44. Matsunaga K, Murata H, Mizoguchi T, Nakahira A. Mechanism of incorporation of zinc into hydroxyapatite. *Acta Biomater*. 2010;6(6):2289–2293. doi:10.1016/j.actbio.2009.11.029
45. Li MO, Xiao XF, Liu RF, Chen CYH, Huang L. Structural characterization of zinc-substituted hydroxyapatite prepared by hydrothermal method. *J Mater Sci Mater Med*. 2008;19(2):797–803. doi:10.1007/s10856-007-3213-4
46. Shepherd D, Best SM. Production of zinc-substituted hydroxyapatite using various precipitation routes. *Biomed Mater*. 2013;8(2):025003. doi:10.1088/1748-6041/8/2/025003
47. Webster TJ, Ergun C, Doremus RH, Bizios R. Hydroxylapatite with substituted magnesium, zinc, cadmium and yttrium II. Mechanisms of osteoblast adhesion. *J Biomed Mater Res*. 2002;59(2):312–317. doi:10.1002/jbm.1247
48. Termine JD, Posner AS. Infra-red determination of the percentage of crystallinity in apatitic calcium phosphates. *Nature*. 1966;211(5046):268–270. doi:10.1038/211268a0
49. Sahadat H, Samina A. FTIR spectrum analysis to predict the crystalline and amorphous phases of hydroxyapatite: a comparison of vibrational motion to reflection. *RSC Adv*. 2023;13:14625–14630.
50. Kaflak A, Kolodziejski W. Complementary information on water and hydroxyl groups in nanocrystalline carbonated hydroxyapatites from TGA, NMR and IR measurements. *J Kol Struct*. 2011;990:263–270.
51. Kolmas J, Kalinowski E, Wojtowicz A, Kolodziejski W. Mid-infrared reflectance microspectroscopy of human molars: chemical comparison of the dentin–enamel junction with the adjacent tissues. *J Mol Struct*. 2010;966:113–121.
52. Kolmas J, Kolodziejski W. Concentration of hydroxyl groups in dental apatites: a solid-state ^{1}H MAS NMR study using inverse ^{31}P → ^{1}H cross-polarization. *Chem Commun*. 2007;4390–4392.
53. Gomes S, Nedelec J-M, Renaudin G. On the effect of temperature on the insertion of zinc into hydroxyapatite. *Acta Biomater*. 2012;8(3):1180–1189.
54. Pajchel L, NMR KWS-SMAS. TEM, and TGA studies of structural hydroxyl groups and water in nanocrystalline apatites prepared by dry milling. *J Nanopart Res*. 2013;15:1868.
55. Sugimoto K, Zhou Y, Galindo TGP, Kimura R, Tagaya M. Investigation of surface layers on biological and synthetic hydroxyapatites based on bone mineralization process. *Biomimetics*. 2023;28(2):184. doi:10.3390/biomimetics8020184
56. Chappel H, Duer M, Groom N, Pickard C, Bristowe P. Probing the surface structure of hydroxyapatite using NMR spectroscopy and first principles calculations. *Phys Chem Chem Phys*. 2008;10:600–606.
57. Kolmas J, Kolodziejski W. Inverse ^{31}P → ^{1}H NMR cross-polarization in hydrated nanocrystalline calcium hydroxyapatite. *Chem Phys Lett*. 2012;554:128–132.
58. Yu Y, Guo H, Pujari-Palmer M, et al. Advanced solid-state 1H/31P NMR characterization of pyrophosphate-doped calcium phosphate cements for biomedical applications: the structural role of pyrophosphate. *Ceram Int*. 2019;45(16):20642–20655.
59. Jäger C, Welzel T, Meyer-Zaika W, Epple M. A solid-state NMR investigation of the structure of nanocrystalline hydroxyapatite. *Magn Reson Chem*. 2006;44:573–580. doi:10.1002/mrc.1774
60. Koutsopoulos S. Synthesis and characterization of hydroxyapatite crystals: a review study on the analytical methods. *J Biomed Mater Res*. 2002;62(4):600–612. doi:10.1002/jbm.10280

61. Mayer I, Apfelbaum F, Featherstone JDB. Zinc ions in synthetic carbonated hydroxyapatite. *Arch Oral Biol*. 1994;39(1):87–90.
62. Akazawa H. Characterization of crystallographic orientation and lattice disorder in hydroxyapatite thin films by Raman scattering. *Ceram Int*. 2022;48(1):624–631.
63. Anwar A, Akbar S, Sadiqa A, Kazmi M. Novel continuous flow synthesis, characterization and antibacterial studies of nanoscale zinc substituted hydroxyapatite bioceramics. *Inorg Chim Acta*. 2016;453:16–22.
64. Frost RL. An infrared and Raman spectroscopic study of natural zinc phosphates. *Spectrochim, Acta A Mol, Biomol, Spectrosc*. 2004;60(7):1439–1445. doi:10.1016/j.saa.2003.08.009
65. Liu HY, Gale JR, Reynolds IJ, Weiss JH, Aizenman E. The multifaceted roles of zinc in neuronal mitochondrial dysfunction. *Biomedicines*. 2021;9(5):489. doi:10.3390/biomedicines9050489
66. Mohan Babu M, Venkateswara Rao P, Singh RK, et al. ZnO incorporated high phosphate bioactive glasses for guided bone regeneration implants: enhancement of in vitro bioactivity and antibacterial activity. *J Mater Res Technol*. 2021;15:633–646. doi:10.1016/j.jmrt.2021.08.020
67. Yang Q, Yang J, Liu X, et al. Crosstalk between the mitochondrial dynamics and oxidative stress in zinc-induced cytotoxicity. *Biol. Trace Elem Res*. 2023;201:4419–4428.